ADVANCED PHOTONICS RESEARCH
Open Access
www.adpr-journal.com

Exploring the Role of Artificial Intelligence in Precision Photonics: A Case Study on Deep Neural Network-Based fs Laser Pulsed Parameter Estimation for MoO_x Formation

*Jose R. Paredes-Miguel, Miroslava Cano-Lara, Andres A. Garcia-Granada, Andres Espinal, Marcos J. Villaseñor-Aguilar, Leonardo Martinez-Jimenez, and Horacio Rostro-Gonzalez**

Ultrafast pulsed laser technology presents unique challenges and opportunities in material processing and characterization for precision photonics. Herein, an experiment is conducted involving the use of an ultrafast pulsed laser to irradiate a molybdenum film, inducing oxide formation. A total of 54 experiments are performed, varying the laser irradiation time and per-pulse laser fluence, resulting in a database with diverse oxide formations on the material. This dataset is further expanded numerically through interpolation to 187 samples. Subsequently, eight different deep neural network models, each with varying hidden layers and numbers of neurons, are employed to characterize the laser behavior with different parameters. These models are then validated numerically using three different learning rates, and the results are statistically evaluated using three metrics: mean squared error, mean absolute error, and R^2 score.

1. Introduction

In recent decades, the advent of ultrafast pulsed laser technology has revolutionized various fields, from materials science to biomedical engineering, owing to its exceptional precision and minimal thermal damage.[1–6] These ultrafast lasers, characterized by pulse durations on the order of femtoseconds to picoseconds, offer unparalleled capabilities for material processing and manipulation at the micro- and nanoscale levels.[7–10] One particularly intriguing application of ultrafast pulsed lasers is in the modification and characterization of thin films,[11–14] which play crucial roles in numerous technological advancements including microelectronics, optoelectronics, and surface engineering.[15–17]

Among the materials commonly utilized in thin film applications, molybdenum (Mo) stands out for its unique combination of mechanical, electrical, and thermal properties.[18–22] Thin molybdenum films find extensive use in electronic devices, catalysis, and solar energy conversion systems.[23–25] Understanding the effects of ultrafast pulsed laser irradiation on these films is of paramount importance for optimizing laser processing techniques and harnessing their full potential in various applications.[26–28]

Exploring the laser–material interaction area using traditional techniques, which involve studying the interaction of a physical laser with real materials, can take weeks or months to achieve significant laboratory progress. Conventional methods for assessing the effects of laser irradiation on materials often involve time-consuming experimental procedures and extensive post-processing analysis.[29] Understanding pattern recognition in phase transformation or etching in materials using ultrashort pulse lasers demands precision, versatility, and control. The rapid evolution of Artificial Intelligence (AI), particularly in the fields of Machine Learning (ML), Deep

J. R. Paredes-Miguel, H. Rostro-Gonzalez
Department of Electronics Engineering
DICIS - University of Guanajuato
36885 Salamanca, Mexico
E-mail: horacio.rostro@iqs.url.edu

J. R. Paredes-Miguel
Institute for Research in Technology
Universidad Pontificia Comillas
28015 Madrid, Spain

The ORCID identification number(s) for the author(s) of this article can be found under https://doi.org/10.1002/adpr.202400113.

DOI: 10.1002/adpr.202400113

M. Cano-Lara, M. J. Villaseñor-Aguilar
Department of Mechatronics Engineering
National Technological Institute of Mexico/ITS of Irapuato
36821 Irapuato, Mexico

A. A. Garcia-Granada, H. Rostro-Gonzalez
GEPI Research Group
School of Engineering - IQS
Universitat Ramon Llull
Via Augusta 390, 08017 Barcelona, Spain

A. Espinal
Department of Organizational Studies
University of Guanajuato
36250 Guanajuato, Mexico

L. Martinez-Jimenez
Department of Multidisciplinary Studies
DICIS University of Guanajuato
38940 Yuriria, Mexico

Learning models (DL), and Convolutional Neural Networks (CNNs),[30] facilitates the optimization of parameters in experimental testing.

These DL techniques are capable of addressing the complex physics involved in the fields of optics and photonics, utilizing various architectural models for specific tasks.[31,32] They facilitate data analysis, parameter optimization, and the generation of predictive algorithms. For example, they can solve problems in photonic design,[33] specifically in the application of silicon photonics,[34] and in the creation of structuring/texturing surfaces like laser-induced periodic surface structures (LIPSS).[35] These advancements have paved the way for more efficient and accurate characterization techniques in materials science. DL models excel at extracting complex patterns and features from large datasets, making them well-suited for analyzing intricate morphological and structural changes induced by laser irradiation.[36–39]

The integration of DL with photonic in particular ultrafast laser processing holds immense potential for accelerating the characterization process and gaining deeper insights into the intricate phenomena occurring at the nanoscale level. The findings of this study are expected to not only advance our fundamental understanding of laser-material interactions but also facilitate the development of innovative strategies for precise control and manipulation of thin molybdenum films for diverse technological applications.

The rest of the article is divided as follows: in Section 2, the scope of this work is presented. In Section 3, the materials and methods used are introduced, highlighting the experimental setup designed to collect the data that will be subsequently analyzed using deep neural networks (DNNs). Subsequently, in Section 4, the results of this research are presented through statistical metrics applied to the results, and conclusions are drawn in Section 6.

2. Scope of This Study

The aim of this research is to explore the application of AI, particularly DNNs, for analyzing and estimating irradiation parameters in materials such as molybdenum using femtosecond pulsed laser technology. By leveraging numerical tools, we seek to perform comprehensive computational analyses to identify optimal parameters before conducting direct material irradiation. This approach not only aims to streamline the process and reduce costs but also enables the exploration of a wide range of parameters without the need for extensive physical optical experiments. Our research aspires to develop more efficient and cost-effective material irradiation techniques, thereby advancing various technological applications in precision photonics. By training DNNs with various configurations on a comprehensive dataset that includes both real and numerically generated data—encompassing laser-processed samples with varying parameters such as irradiation time, per-pulse fluence, and the diameter of oxide generated on the surface of the molybdenum film—we establish a robust framework. Through systematic experimentation and computational modeling, our objective is to elucidate the underlying mechanisms governing laser-material interactions and to clarify the influence of process parameters on the characterization of thin films.

3. Experimental Section

3.1. Optical Experimental Setup

The experimental setup consists of three stages, as illustrated in **Figure 1**. Firstly, the goal is to determine the properties of the spatial Gaussian profile provided by femtosecond laser pulses. To analyze the laser beam parameters and the fixed spot position on the molybdenum films, an image relay with a CCD camera is acquired. The Ti:sapphire fs laser (with a pulse width of 60 fs, repetition rate of 70 MHz, and a wavelength of 800 nm) offers energy ranging from 1.4 to 4.2 nJ and fluence per pulse from 1.4 to 4.2 mJ cm^{-2}, along with exposure times between 2 and 1200 s, resulting in a collection of irradiation spots on the molybdenum film.[11,13]

Next, to acquire a rich variety of phase transformations for MoO_x, we aim to analyze the integration of the experimental laser parameters and the images of the irradiation spots using a DNN. We explore this in conjunction with different configurations of DNNs,[27] which implies changing the number of neurons and layers in order to find an optimal solution.

The range of color present in the concentric rings of irradiated molybdenum layers indicates specific stoichiometries of MoO_x. These micron-scale phases prompt us to explore innovative techniques using such kind of networks.

3.2. Experimental Data and Material Characterization

Based on the experimental setup illustrated in Figure 1, the schematic diagram in **Figure 2** represents the interaction phenomenon between the fs laser parameters and the properties of a 500 nm thick molybdenum metal film in an air environment. It is crucial to identify the importance of working with specific parameters of a laser oscillator. In this study, we consider the properties produced by a Ti:Sapphire laser with a wavelength of 800 nm, output pulses of 60 fs, per-pulse energy of 6 nJ, and a repetition rate of 70 MHz, featuring a Gaussian beam profile. The fixed irradiation matrix S_{ij} generated with 54 points on the Mo film with normal incidence will depend on both the laser parameters and the duly controlled exposure time. Although the microprocessing lens used is a convergent or positive lens with a focal length of 35 mm, the laser beam exhibits a slightly elliptical shape, representing irradiation points with dimensions dependent on a major and minor axis (12.85 and 10.36 μm), respectively, acquired at $FW1\frac{1}{e^2}M$. It is important to note that the results of the MoO_x phase change in the interaction region are below 4% of the ablation threshold fluence, thus achieving the synthesis of multiphases of MoO_x. The wide range of stoichiometries related to the color pattern, with the help of optical microscopy techniques (color rings as irradiation progresses), SEM (morphological changes with micro/nanostructuring), and micro-Raman spectroscopy (varying sub-stoichiometric phases), highlight the rapid evolution of the molybdenum layer as it interacts with each exposure during the pulsed laser processing. It is noteworthy in each representative matrix S_{69}, the

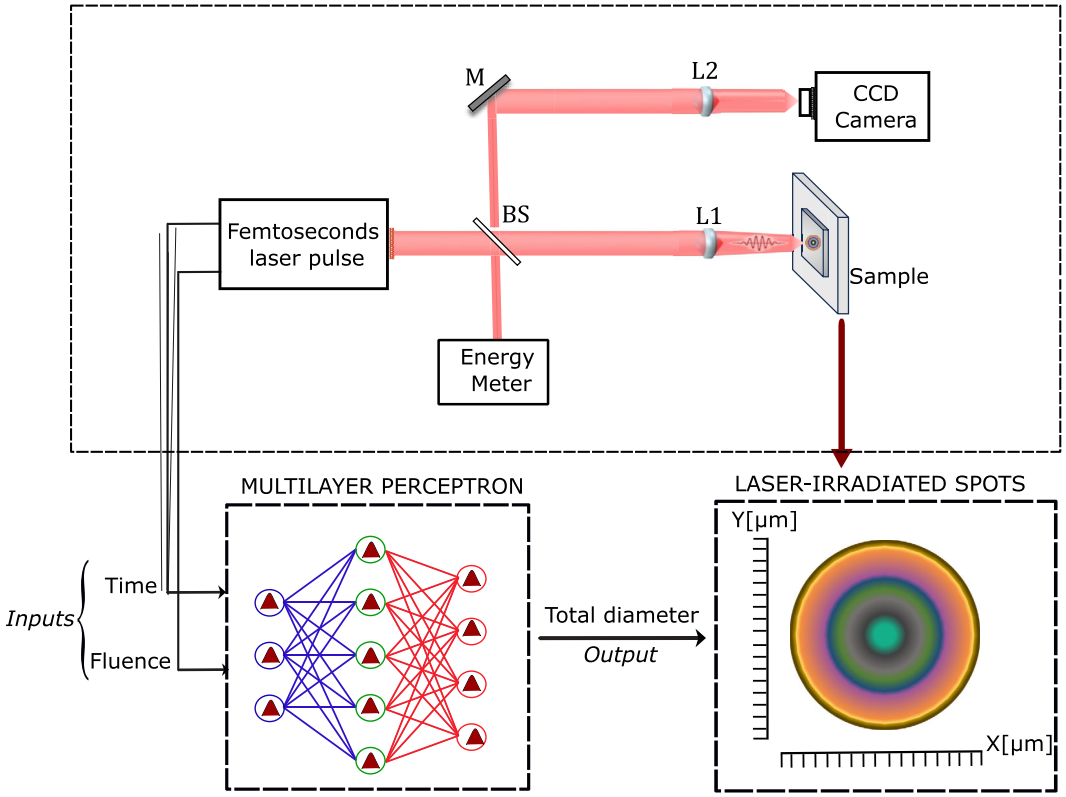

Figure 1. Schematic illustration of DL with interaction between femtosecond laser pulse and surface of molybdenum thin film.

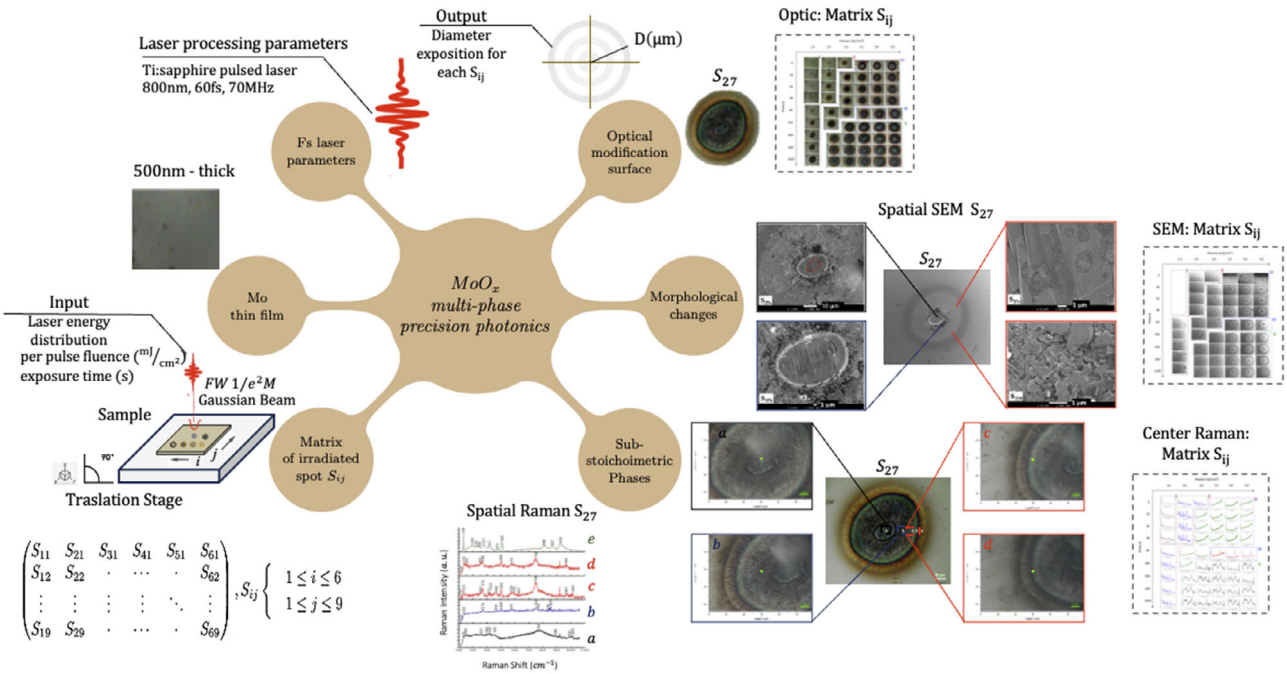

Figure 2. Detailed diagram schematic between fs laser parameters, Mo thin film properties, matrix of irradiated spot S_{ij}, optical microscopy, scanning electron microscopy, and micro-Raman spectroscopy characterization of the irradiated regions MoO_x. Adapted from ref. [13].

distinctive features in the central area where there is strong optical absorption and a strong electric field, followed by the generation of concentric color rings (dark red, blue, green, light red, and black) (see **Figure 3**). This effect is due to heat diffusion and the increase in per-pulse fluence as the exposure time varies. Similarly, these features are related to the crystalline structure at the center and the spatially resolved Raman spectra, which exhibit phases such as *a*-MoO_x, *m*-MoO_2, *o*-$Mo_{18}O_{52}$, *m*-Mo_8O_{23}, and α-MoO_3. Additionally, it is possible to identify their morphological and textural features for each MoO_x, including crystals like nanobars, micro- and nano-sized structures, polyhedral particles, and granular structures.[11,13] See **Table 1** for a graphical representation of this data provided in **Figure 4**.

3.3. Data Augmentation

Data augmentation is a crucial step undertaken using the data collected during our experiments. This process aims to enhance the robustness and generalization capabilities of the DNN. As is widely recognized, artificial neural networks, especially deep nets, thrive on large volumes of data for optimal performance.

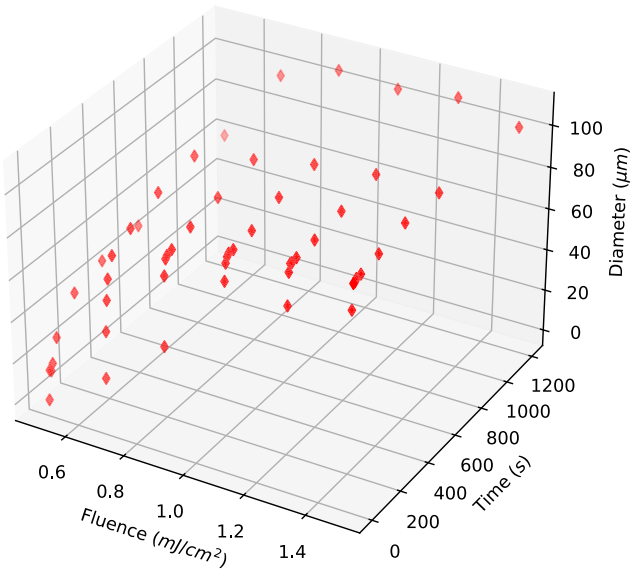

Figure 4. Experimental data plot.

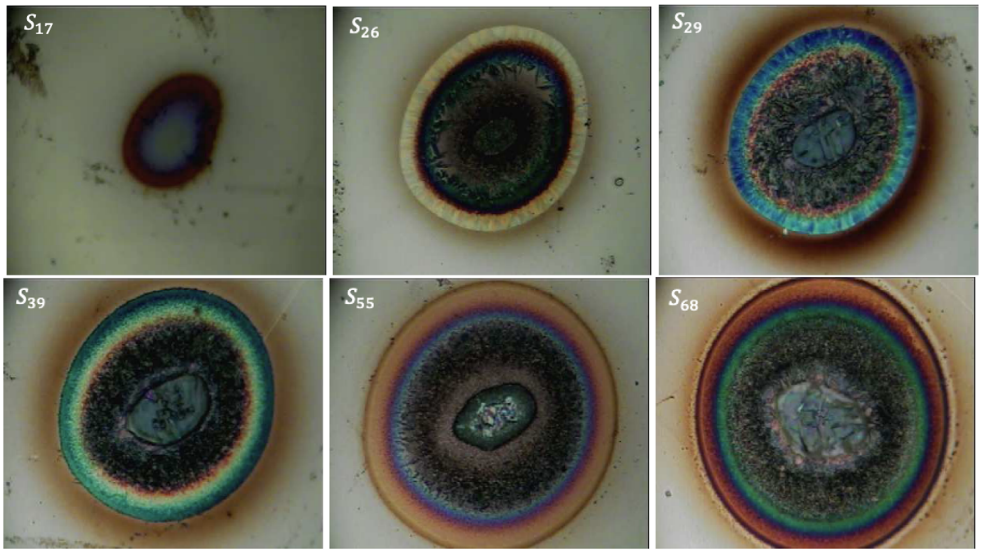

Figure 3. Samples of oxides shown in optical micrographs generated from laser irradiation on molybdenum film. Adapted from ref. [13].

Table 1. Experimental data: diameters (in μm) generated in molybdenum films from laser irradiation under varied conditions of irradiation time and fluence. Adapted from ref. [13].

Fluence [mJ cm^{-2}]	Time [s]								
	2	10	20	30	60	180	360	600	1200
1.4	0.0	14.10	13.05	16.10	26.84	41.05	45.68	48.52	59.26
1.9	19.57	41.57	55.78	65.26	74.42	80.00	86.42	90.10	96.10
2.5	43.68	76.31	83.57	84.63	85.47	88.84	92.00	96.1	105.89
3.1	82.73	90.52	92.84	93.89	93.68	95.26	100.00	101.57	104.21
3.6	80.00	94.73	98.10	97.89	98.31	99.15	101.68	104.73	107.57
4.2	86.63	98.10	98.21	99.15	99.26	101.15	104.42	104.21	101.05

Table 2. Augmented data: through interpolation, we expanded our dataset from 54 real diameters to 187 (including the 54 real and 133 generated diameters).

Fluence [mJ cm^{-2}]	Time [s]																
	2	6	10	15	20	25	30	45	60	120	180	270	360	480	600	900	1200
1.40	0.0	7.05	14.10	13.57	13.05	15.57	16.10	21.47	26.84	33.94	41.05	43.36	45.68	47.10	48.52	56.89	59.26
1.65	9.78	18.81	27.83	31.12	34.41	37.54	40.68	45.65	50.63	55.57	60.52	63.28	66.05	67.68	69.31	73.49	77.68
1.90	19.57	30.57	41.57	48.67	55.78	60.52	65.26	69.84	74.42	77.21	80.00	83.21	86.42	88.26	90.10	93.10	96.10
2.30	31.62	45.28	58.94	63.30	69.67	72.31	74.94	77.44	79.94	82.18	84.42	86.81	89.21	91.15	93.10	97.04	100.99
2.50	43.68	59.99	76.31	79.94	83.57	84.10	84.63	85.05	85.47	87.15	88.84	90.42	92.00	94.05	96.10	100.99	105.89
2.80	63.20	73.31	83.41	85.81	88.20	88.73	89.26	89.41	89.57	90.81	92.05	94.02	96.00	97.41	98.83	101.94	105.05
3.10	82.73	86.62	90.52	91.68	92.84	93.36	93.89	93.78	93.68	94.47	95.26	97.63	100.00	100.78	101.57	102.89	104.21
3.35	81.36	86.99	92.62	94.04	95.47	95.68	95.89	95.94	95.99	96.60	97.20	99.02	100.84	101.99	103.15	104.52	105.89
3.60	80.00	87.36	94.73	96.41	98.10	97.99	97.89	98.10	98.31	98.73	99.15	100.41	101.68	103.20	104.73	106.15	107.57
3.90	83.31	89.86	96.41	97.28	98.15	98.33	98.52	98.65	98.78	99.46	100.15	101.60	103.05	103.76	104.47	104.39	104.31
4.2	86.63	92.36	98.10	98.15	98.21	98.68	99.15	99.20	99.26	100.20	101.15	102.78	104.42	104.31	104.21	102.63	101.05

To meet this requirement, we employed interpolation techniques to generate additional meaningful data from real experimental observations. The outcomes of this augmentation stage are presented in **Table 2** and depicted in **Figure 5**.

3.4. Deep Neural Networks

Regarding data processing, we have chosen to utilize a DNN.[30] This approach enables the mapping of the dataset and the creation of a model that can be validated using parameters different from those employed in the real experiment. By virtue of being a model that generalizes data behavior, we can numerically explore various configurations before validating them in a real experiment, which involves resource utilization. This strategy minimizes errors and material wastage.

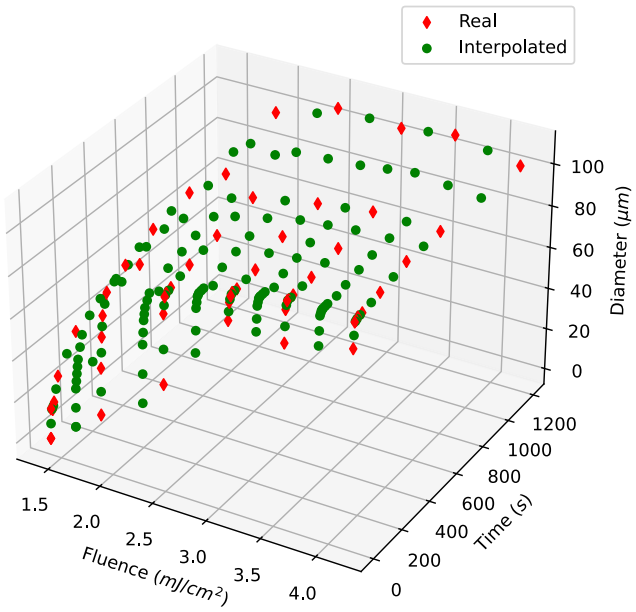

Figure 5. Augmented experimental data. Red dots correspond to the original (experimental data) and green dots correspond to artificially generated data.

Theoretically and computationally, a DNN is composed of a specific number of layers, where the inputs correspond to the number of classes or parameters to be modeled, and the output depends on the value(s) to be determined from these parameters. In our case, for the input layer, we have two variables: the laser irradiation time on the material and the per-pulse fluence. Regarding the output, it corresponds to the MoO_x formation diameter generated by the laser with these parameters. In addition to these layers, a DNN is constructed with hidden layers, which are responsible for finding relationships in the data through a training mechanism. The number of layers and neurons in them are typically determined through an empirical process. In this regard, we have explored different configurations, which are presented in **Table 3**.

Figure 6 depicts a graphical representation of a DNN architecture, detailing the number of hidden layers and neurons in these layers as presented in Table 3. The rationale behind this investigation into the number of hidden layers and neurons stems from the recognition that a more complex

Table 3. Network configurations.

Model	Number of neurons per hidden layer						
	Layer 1	Layer 2	Layer 3	Layer 4	Layer 5	Layer 6	Layer 7
DNN 1	32	64	32	–	–	–	–
DNN 2	64	128	64	32	–	–	–
DNN 3	64	128	64	32	16	–	–
DNN 4	128	64	32	16	–	–	–
DNN 5	256	128	54	32	–	–	–
DNN 6	350	256	128	64	32	–	–
DNN 7	700	525	350	175	88	36	–
DNN 8	700	525	350	175	88	36	18

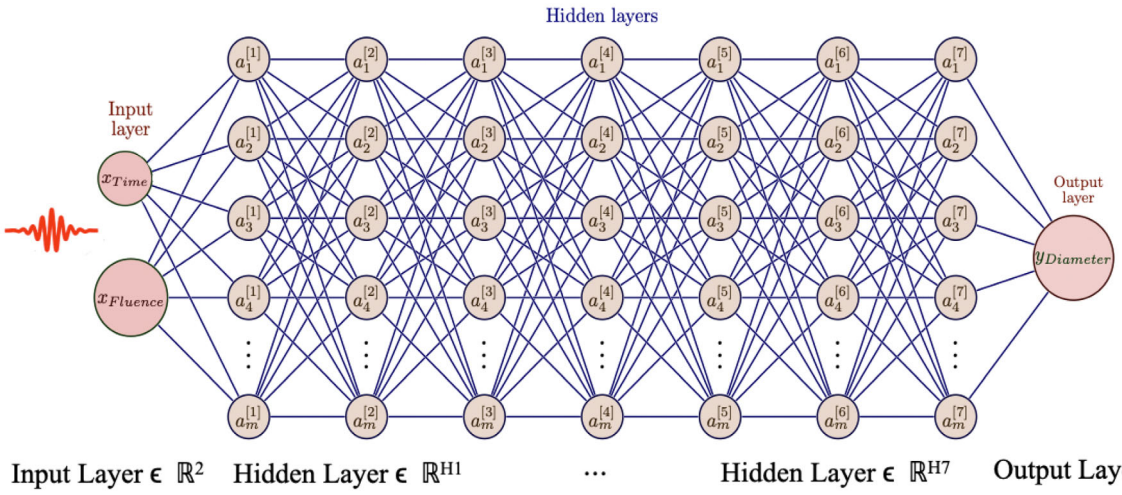

Figure 6. DNN architecture.

architecture demands greater computational resources. However, such resources can be limited, particularly in embedded applications. Thus, our exploration encompasses various neural architectures to provide insights for the development of future applications.

4. Results and Discussion

In terms of results, we will discuss the statistical metrics used in this work. While we have explored a wide variety of neural architectures with different layers and neurons in each of them, the way to evaluate their performance is based on their statistical outcomes, which allow us to understand and observe if the models learned the data behavior well. Moreover, we can determine if these models can provide results with parameters different from those used for training them. In this regard, we first observe the mean squared error (MSE), which represents the average measure of the squared errors between the predicted values by our different models and the actual values in a dataset. It is a measure of the model's fit to the data, where lower MSE values indicate a better fit, as they indicate that the model's predictions are closer to the actual values. In this sense, we can observe in **Table 4** that the DNN2 network with a Nadam optimizer numerically represents the best result since it is 58.47; conversely, the one that performs the worst among the best cases is DNN6 with an AdamW optimizer with a value of 147.01.

Now, focusing on the mean absolute error (MAE) reported in Table 4, we observe that the maximum reported error is 8.45 and the minimum is 4.25. These values are measured in μm and correspond to the same DNN6 and DNN2 architectures, respectively. Additionally, we have good performance in the rest of the architectures, which are highlighted in green in the table.

The following validation conducted aimed to observe the behavior of different architectures and optimizers through the coefficient of determination or R^2 score. With this coefficient, we can determine how well a regression model follows the data behavior. An advantage of using the coefficient of determination (R^2 score) over MSE and MAE lies in its ability to provide a more comprehensive and understandable measure of model performance. While MSE and MAE represent absolute measures of the magnitude of prediction errors, the R^2 score provides a relative measure of the model's ability to explain variability in the data. The R^2 score measures the proportion of variance in the data explained by the model. A higher R^2 score indicates that the model can explain a greater amount of variability in the data, suggesting a better model fit. This allows for a more intuitive interpretation of model performance, as it is expressed as a percentage of the total variance in the data that can be explained by the model. Thus, we can observe in **Table 5** that the DNN2

Table 4. Comparison of MSE and MAE among various optimizers.

Optimizer	DNN 1		DNN 2		DNN 3		DNN 4		DNN 5		DNN 6		DNN 7		DNN 8	
	MSE	MAE	MSE	MAE	MSE	MAE	MSE	MAE	MSE	MAE	MSE	MAE	MSE	MAE	MSE	MAE
Adelta	8539.46	78.80	1320.65	22.04	6199.55	63.94	7444.72	70.92	8201.76	77.00	256.17	12.29	273.11	12.85	287.26	12.95
Adagrad	2766.14	44.95	246.78	12.97	260.63	13.51	250.98	12.73	228.73	11.97	284.77	14.18	223.46	12.74	207.88	11.95
Adam	130.73	8.31	81.10	5.68	249.19	11.58	113.43	9.55	59.39	6.07	171.76	8.54	83.78	6.35	120.29	9.22
AdamW	138.22	8.70	69.50	5.67	80.50	7.50	150.07	10.15	87.40	6.82	147.01	8.45	74.65	4.70	113.56	7.67
Nadam	273.73	13.73	58.47	4.25	61.31	5.37	90.67	7.34	65.37	6.14	175.22	9.79	68.02	6.11	138.51	8.90
RMSprop	154.61	11.12	277.50	9.90	130.41	8.26	257.50	11.98	1119.05	20.23	166.21	10.33	183.4	9.83	145.91	9.98

Table 5. Statistical results: coefficient of determination (R^2 score) for the 8 DNN architectures using various optimizers.

Optimizer	DNN 1	DNN 2	DNN 3	DNN 4	DNN 5	DNN 6	DNN 7	DNN 8
Adelta	−13.76	−1.28	−9.71	−11.86	−13.17	0.56	0.53	0.5
Adagrad	−3.78	0.57	0.55	0.57	0.60	0.51	0.61	0.64
Adam	0.77	0.86	0.49	0.8	0.90	0.70	0.86	0.79
AdamW	0.76	0.88	0.86	0.74	0.85	0.75	0.87	0.80
Nadam	0.53	0.90	0.89	0.84	0.89	0.70	0.88	0.76
RMSprop	0.73	0.52	0.77	0.55	−0.93	0.71	0.68	0.75

Table 6. Behavior of MSE and MAE for three different learning rates across the 8 DNN models.

Model	$lr = 0.001$		$lr = 0.0001$		$lr = 0.00001$	
	MSE	MAE	MSE	MAE	MSE	MAE
DNN 1	230.98	12.86	96.8	8.47	141.35	9.37
DNN 2	59.83	6.41	77.58	5.79	130.53	6.24
DNN 3	109.7	7.93	85.93	6.51	71.73	5.61
DNN 4	93.01	6.93	45.75	4.82	59.59	5.13
DNN 5	208.51	9.6	43.19	4.98	48.98	5.1
DNN 6	110.87	7.86	62.97	5.22	88.25	5.85
DNN 7	60.23	5.42	31.08	4.00	27.86	3.58
DNN 8	122.13	8.18	34.48	3.63	12.56	2.42

network with the Nadam optimizer, along with the DNNy network and Adam optimizer, exhibits the best performance. This consistency supports previous results, where the combination of DNN2 and Nadam optimizer also showed the best performances in MSE and MAE.

Finally, **Table 6** presents the MSE and MAE errors obtained by varying the learning rate across three different values for the 8 DNN configurations. The learning rate facilitates precise adjustments in the synaptic weights of the network. However, opting for a very small value prolongs the convergence time toward an optimal solution and escalates computational expenses. In this experiment, the most optimal configuration is identified in DNN8 with a learning rate of 0.00001.

5. Physical Significance of the Results

It is well known that real-world machine learning problems suffer from data scarcity and class imbalance, among other issues. The former is particularly relevant when using DL algorithms, as large amounts of data are required to build an appropriate model and mitigate potential underfitting or overfitting problems.[40] Currently, for problems with limited samples, data augmentation is the most suitable option as it increases the volume, quality, and diversity of the training dataset, thus enabling DL models to perform well on unseen samples.[41,42]

One of the most critical aspects when attempting to replicate or model physical phenomena using AI is its ability to capture the various dynamics that such phenomena can produce. Thus, it is desirable for augmented training dataset to possess sample diversity, allowing models to handle noise and deviations in the data, while ensuring that data quality does not degrade to the point of diminishing performance on real samples.[41] To evaluate the reliability of our proposed architectures and the quality of the interpolated data, we extended our research by generating additional synthetic data. The newly interpolated data are presented in **Table 7** and **8**.

To assess the value of interpolation-based augmented data in the context of predicting the physical phenomenon of laser irradiation on materials, we conducted a series of experiments using 8 DNN models and 6 optimizers, training the architectures exclusively on the synthetic dataset. After training the architectures with synthetic data, we validated their performance using experimental data.

A total of 48 experimental configurations were defined, and 54 independent runs were executed for each. For every single run, there were calculated mean absolute error (MAE), mean squared error (MSE), and R^2 metrics for both the training and testing sets. A lower MAE indicates that the model is able to more accurately predict the effects of laser irradiation on the material, which is directly tied to the precision of material processing in real-world applications. In addition, MSE is another important metric that quantifies the difference between the predicted and actual values, with a greater penalty on larger errors. A lower MSE suggests that the model is capturing the relationship between laser parameters and material responses, such as oxide formation or other surface modifications, with high precision. This accuracy is essential in material processing, where small deviations in parameter settings can lead to significant discrepancies in the final material properties. By minimizing MSE, the model aids in optimizing laser parameters, enhancing material quality, and reducing the likelihood of defects. Furthermore, *R*-squared (R^2) measures the proportion of variance explained by the model. A higher R^2 value indicates that the model effectively captures the underlying physical processes, such as the interaction of the laser with the material, making it a strong predictor for material responses like oxide formation. This is crucial for industrial processes like thin-film deposition, surface modification, and laser cleaning, where precise control over material properties is essential. A high R^2 demonstrates that the model not only predicts outcomes with high accuracy but can also be reliably used in real-world applications, optimizing laser treatments to improve material durability, surface quality, and overall process efficiency.

The result sets were statistically analyzed to validate whether there were substantial differences when using the 48 different configurations. The metric chosen for the statistical analysis was the MSE of the testing data, as we are interested in models with high generalization capability, low error rates, and MSE penalizes large differences between target and predicted values. According to the Shapiro–Wilk normality test, some result sets were found to be non-normally distributed. Consequently, the Friedman rank sum nonparametric test was applied to verify if there were statistically significant differences in the performance of the different configurations. The results of the Friedman test indicate a statistically significant

Table 7. Augmented data generated through interpolation for validating physical significance (part 1).

Fluence [mJ cm^{-2}]	Time [s]									
	1.40	1.53	1.65	1.78	1.90	2.10	2.30	2.40	2.50	2.65
2	0.00	4.89	9.79	14.68	19.57	25.60	31.63	37.65	43.68	53.44
6	7.05	12.93	18.81	24.69	30.57	37.93	45.28	52.64	60.00	66.65
10	14.10	20.97	27.84	34.70	41.57	50.26	58.94	67.63	76.31	79.86
15	13.58	22.35	31.13	39.90	48.68	56.49	64.31	72.12	79.94	82.88
20	13.05	23.73	34.42	45.10	55.78	62.73	69.68	76.62	83.57	85.89
25	14.58	26.06	37.55	49.03	60.52	66.42	72.31	78.21	84.10	86.42
30	16.10	28.39	40.68	52.97	65.26	70.10	74.95	79.79	84.63	86.95
45	21.47	33.56	45.66	57.75	69.84	73.64	77.45	81.25	85.05	87.23
60	26.84	38.74	50.63	62.53	74.42	77.18	79.95	82.71	85.47	87.52
120	33.95	44.76	55.58	66.39	77.21	79.70	82.18	84.67	87.16	88.98
180	41.05	50.79	60.53	70.26	80.00	82.21	84.42	86.63	88.84	90.45
270	43.37	53.33	63.29	73.25	83.21	85.01	86.82	88.62	90.42	92.22
360	45.68	55.87	66.05	76.24	86.42	87.82	89.21	90.61	92.00	94.00
480	47.10	57.39	67.68	77.97	88.26	89.71	91.16	92.60	94.05	95.73
600	48.52	58.92	69.31	79.71	90.10	91.60	93.10	94.60	96.10	97.47
900	53.89	63.69	73.50	83.30	93.10	95.07	97.05	99.02	101.00	101.47
1200	59.26	68.47	77.68	86.89	96.10	98.55	101.00	103.44	105.89	105.47

Table 8. Augmented data generated through interpolation for validating physical significance (part 2).

Fluence [mJ cm^{-2}]	Time [s]										
	2.80	2.95	3.10	3.23	3.35	3.48	3.60	3.75	3.90	4.05	4.20
2	63.21	72.97	82.73	82.05	81.37	80.68	80.00	81.66	83.32	84.97	86.63
6	73.31	76.29	86.63	86.81	87.00	87.18	87.37	88.62	89.87	91.12	92.37
10	83.42	86.97	90.52	91.57	92.63	93.68	94.73	95.57	96.42	97.26	98.10
15	85.81	84.84	91.68	92.86	94.05	95.23	96.42	96.85	97.29	97.72	98.16
20	88.21	90.52	92.84	94.16	95.47	96.79	98.10	98.13	98.16	98.18	98.21
25	88.73	88.10	93.37	94.52	95.68	96.84	98.00	98.17	98.34	98.51	98.68
30	89.26	91.58	93.89	94.89	95.89	96.89	97.89	98.21	98.52	98.84	99.15
45	89.42	89.70	93.79	94.86	95.94	97.02	98.10	98.38	98.65	98.93	99.21
60	89.58	91.63	93.68	94.84	96.00	97.15	98.31	98.55	98.79	99.02	99.26
120	90.81	91.40	94.47	95.54	96.60	97.67	98.73	99.10	99.47	99.84	100.21
180	92.05	93.66	95.26	96.23	97.21	98.18	99.15	99.65	100.15	100.65	101.15
270	94.03	94.93	97.63	98.33	99.02	99.72	100.42	101.01	101.60	102.19	102.79
360	96.00	98.00	100.00	100.42	100.84	101.26	101.68	102.37	103.05	103.74	104.42
480	97.42	98.38	100.79	101.39	102.00	102.60	103.21	103.48	103.76	104.04	104.32
600	98.84	100.20	101.57	102.36	103.15	103.94	104.73	104.60	104.47	104.34	104.21
900	101.94	101.43	102.89	103.71	104.52	105.34	106.15	105.27	104.39	103.51	102.63
1200	105.05	104.63	104.21	105.05	105.89	106.73	107.57	105.94	104.31	102.68	101.05

difference between the groups analyzed ($\chi^2 = 2156.3$, $df = 47$, $p < 2.2 \times 10^{-16}$). Since the p-value is far below the significance threshold of 0.05, we reject the null hypothesis, suggesting that at least one of the result sets differs significantly from the others. This strong evidence highlights meaningful variations in the performance of the 48 configurations.

Since significant statistical differences were found across the 48 result sets, we proceeded to analyze their behavior with respect to the mean and standard deviation of the different metrics for the training and testing sets. The results for each experimental configuration are summarized by their mean and standard deviation, as shown in **Table 9**. Focusing on the

Table 9. Statistical summary of various regression metrics from the 48 proposed DNN models trained exclusively on synthetic data and tested on real data.

Model	MAE				MSE				R^2			
	tr_mean	tr_std	te_mean	te_std	tr_mean	tr_std	te_mean	te_std	tr_mean	tr_std	te_mean	te_std
DNN1-adadelta	1.0931	0.4866	13.7231	0.3187	175.3376	11.9024	278.0188	10.9293	0.6888	0.0211	0.6616	0.0133
DNN1-adagrad	11.1359	0.0808	14.2518	0.7782	189.1812	22.3482	310.4332	32.6326	0.6642	0.0397	0.6222	0.0397
DNN1-adam	4.7287	3.4974	0.6495	4.3427	56.2714	65.2209	96.9126	105.6504	0.9001	0.1158	0.0882	0.1286
DNN1-adamw	4.3589	3.2372	5.9742	4.0127	49.2631	5.9781	8.4076	95.9801	0.9126	0.1061	0.8977	0.1168
DNN1-nadam	3.7102	2.9733	5.3232	0.3631	3.8001	54.0959	67.8848	86.1305	0.9325	0.0096	0.9174	0.1048
DNN1-rmsprop	5.1112	3.7741	6.9627	4.6878	63.8723	71.2076	108.8047	115.4441	0.8866	0.1264	0.8676	0.1405
DNN2-adadelta	10.6158	0.2559	13.5593	0.0168	165.5826	5.5301	268.6963	5.2918	0.7061	0.0098	0.0673	0.0064
DNN2-adagrad	10.2524	0.1354	1.3258	0.2092	158.9042	3.8205	259.7113	0.7043	0.7179	0.0068	0.6839	0.0086
DNN2-adam	0.1367	1.3082	2.2242	1.6323	5.6955	21.8488	12.3544	34.6369	0.9899	0.0388	0.0985	0.0422
DNN2-adamw	1.4221	0.0128	2.2251	1.6016	5.8317	21.6403	12.1972	34.7463	0.9896	0.0384	0.9852	0.0423
DNN2-nadam	1.1131	0.3908	1.8766	0.5259	0.2554	2.8017	6.9105	5.0426	0.9955	0.0005	0.9916	0.0061
DNN2-rmsprop	2.2677	1.1986	2.8112	1.0587	8.7405	8.6165	13.6642	10.2885	0.9845	0.0153	0.9834	0.0125
DNN3-adadelta	10.3271	0.2403	13.3417	0.2129	159.4093	5.8207	261.6197	8.2363	0.0717	0.0103	0.6816	0.0001
DNN3-adagrad	10.1893	0.1353	13.1591	0.2071	156.6471	3.9415	256.0466	6.9183	0.7219	0.0007	0.6884	0.0084
DNN3-adam	1.3388	1.3222	2.1096	1.6419	5.6791	21.8741	11.5884	34.7558	0.9899	0.0388	0.9859	0.0423
DNN3-adamw	1.4187	1.7652	2.2204	2.2581	8.1752	30.6044	16.0637	5.1278	0.9855	0.0543	0.9804	0.0624
DNN3-nadam	1.0333	0.3029	1.7401	0.3437	1.9312	0.9795	5.6161	2.0185	0.9966	0.0017	0.9932	0.0025
DNN3-rmsprop	2.3974	1.0762	0.2919	0.9947	9.3747	7.0596	14.1464	8.3104	0.9834	0.0125	0.9828	0.0101
DNN4-adadelta	0.1044	0.2902	13.4287	0.2151	162.0918	6.6774	264.3839	7.5402	0.7123	0.0119	0.6782	0.0092
DNN4-adagrad	10.1656	0.0656	13.3402	0.0857	16.1606	2.4243	268.5426	5.2458	0.7131	0.0043	0.6731	0.0064
DNN4-adam	0.2488	2.4959	3.5376	3.1152	20.5936	42.4585	36.4147	68.6373	0.9634	0.0754	0.9557	0.0835
DNN4-adamw	1.9402	1.7706	2.8692	2.2319	11.8301	30.2947	22.4646	50.0242	0.0979	0.0538	0.9727	0.0609
DNN4-nadam	2.1319	2.2493	3.1397	2.8078	1.5783	3.6177	29.2568	59.3962	0.0972	0.0642	0.9644	0.0723
DNN4-rmsprop	4.2305	3.1342	5.5741	3.9975	44.6549	58.3062	74.9265	95.9211	0.9207	0.1035	0.9088	0.1167
DNN5-adadelta	10.3167	0.1822	13.3312	0.1512	159.4013	3.9742	261.3733	5.0297	0.0717	0.0071	0.6819	0.0061
DNN5-adagrad	10.0461	0.1235	1.3036	0.1905	154.5738	4.1712	253.3963	7.1296	0.7256	0.0074	0.6916	0.0087
DNN5-adam	1.1724	0.3276	1.9292	0.4118	2.6001	0.1822	7.2468	3.1746	0.9954	0.0032	0.9912	0.0039
DNN5-adamw	1.3341	1.2825	0.0211	1.6112	5.4771	21.5898	1.1658	35.7057	0.9903	0.0383	0.9858	0.0435
DNN5-nadam	1.0091	0.2807	1.7586	0.3119	1.8725	1.0358	5.8143	1.9054	0.9967	0.0018	0.9929	0.0023
DNN5-rmsprop	0.2551	0.1274	3.0851	1.2426	10.3517	12.8571	15.8636	15.2269	0.9816	0.0228	0.9807	0.0185
DNN6-adadelta	0.9967	0.2139	12.9779	0.2418	150.5692	5.8222	24.8306	9.2384	0.7327	0.0103	0.6978	0.0112
DNN6-adagrad	6.8243	0.8951	0.8896	0.1116	81.3997	14.6905	134.8545	24.8173	0.8555	0.0261	0.8359	0.0302
DNN6-adam	0.9121	0.2595	1.5388	0.0293	1.4462	0.7377	4.5551	1.4745	0.9974	0.0013	0.9945	0.0018
DNN6-adamw	0.8956	0.2653	0.1556	0.2818	1.3969	0.6861	4.5249	1.4039	0.9975	0.0012	0.9945	0.0017
DNN6-nadam	0.9952	0.3541	1.5752	0.3205	1.6672	0.9783	4.6374	1.5908	0.0997	0.0017	0.9944	0.0019
DNN6-rmsprop	2.8696	1.4022	3.3047	1.2694	11.7742	9.6979	16.0942	1.0232	0.9791	0.0172	0.9804	0.0125
DNN7-adadelta	9.1912	0.3895	12.0529	0.4544	129.6454	10.1878	215.0242	15.8463	0.7699	0.0181	0.7383	0.0193
DNN7-adagrad	3.2244	0.2672	4.1624	0.2662	26.7606	4.2462	43.3693	5.6557	0.9525	0.0075	0.9472	0.0069
DNN7-adam	0.8206	0.3704	1.4467	0.3391	1.2088	1.0271	4.0215	0.0161	0.9979	0.0018	0.9951	0.0002
DNN7-adamw	0.8365	0.3319	1.4562	0.2771	1.2153	0.8141	4.0042	1.1836	0.9978	0.0014	0.9951	0.0014
DNN7-nadam	1.1969	0.7447	1.6909	0.6006	2.4808	2.9283	5.0285	3.0138	0.9956	0.0052	0.9939	0.0037
DNN7-rmsprop	2.9582	1.3555	3.1558	1.3087	12.3069	9.6948	14.9317	10.9414	0.9782	0.0172	0.9818	0.0133
DNN8-adadelta	8.5705	0.0754	11.3285	0.8868	115.2731	16.9587	19.2488	26.7471	0.7954	0.0301	0.7657	0.0326
DNN8-adagrad	0.3175	0.3024	4.1418	0.2739	25.7639	5.0112	42.3262	6.5047	0.9543	0.0089	0.9485	0.0079
DNN8-adam	0.9324	0.4659	1.5871	0.0445	1.5071	1.5259	4.6171	0.2129	0.9973	0.0027	0.9944	0.0026

Table 9. Continued.

Model	MAE				MSE				R^2			
	tr_mean	tr_std	te_mean	te_std	tr_mean	tr_std	te_mean	te_std	tr_mean	tr_std	te_mean	te_std
DNN8-adamw	0.8223	0.3025	1.4568	0.2605	1.1703	0.7479	4.0136	1.0754	0.9979	0.0013	0.9951	0.0013
DNN8-nadam	1.1462	0.6266	1.6617	0.5414	2.2478	2.1841	4.9574	2.6857	0.0996	0.0039	0.0994	0.0033
DNN8-rmsprop	3.2859	1.2929	3.6129	1.3686	14.2312	10.1312	18.5358	12.5189	0.9747	0.0018	0.9774	0.0152

MSE of the testing data, DNN7 with the AdamW optimizer (in green) achieved the best mean result, closely followed by DNN9 with the AdamW optimizer (in yellow), which had the lowest standard deviation. Both models show similar values across all measured statistics for the training and testing sets; however, we selected DNN7 as the best model due to its simpler topology. It is worth mentioning that by observing the mean and standard deviation of MAE for both training and testing data from both models, there are insights suggesting that their overall behavior does not exhibit overfitting. The worst performance is obtained with DNN1 using the Adagrad optimizer (in red), which has the highest mean MSE, and DNN1 with the RMSprop optimizer (in orange), which shows the highest standard deviation. Regarding the DNN1 with Adagrad model, it can be argued that it suffers from underfitting since, in general, it fails to adequately model the data and shows moderate variability across several runs. The DNN1 with RMSprop model shows lower mean MSE values than DNN1 with Adagrad but has a higher standard deviation, making it an unstable model.

Although the aforementioned experimentation is unconventional, it allows for the validation of the viability of interpolated-based generated data for the purpose of this research. We can observe that generated data can produce models with good generalization capability for unseen real data, as studied and analyzed in ref. [43], where several configurations and proportions of real and synthetic data were used for training DL models and testing on both real and synthetic data, showing that augmentation techniques improve the accuracy and generalization of DL models.

Following more conventional experimentation, we proceed to implement Leave-One-Out Cross-Validation (LOOCV). This technique is useful for testing and comparing machine learning models on small datasets.[20] Basically, LOOCV generates disjoint training and testing datasets by using all but one sample as the training set and the remaining one as the testing set. This process is repeated as many times as there are samples in the original dataset, ensuring that each sample is used as a test set exactly once throughout the entire validation process. For our implementation, LOOCV is applied exclusively to the real data, resulting in 54 runs per DNN model. However, in each individual run of LOOCV, the training set is augmented with the entire interpolated-based synthetic data to make the models more robust. As in the previous experiment, we performed statistical tests to verify significant differences in the behaviors of the proposed models. The regression metric was, once again, MSE on the testing data. According to the Shapiro–Wilk normality test, all result sets were found to be non-normally distributed. The results of the Friedman rank sum test indicate a statistically significant difference among the result sets. The test statistic ($\chi^2 = 1042.5$, $df = 47$, $p < 2.2 \times 10^{-16}$) is far below the significance threshold of 0.05. This strongly suggests that there are significant differences between the resulting test.

As previously done, we analyzed the performance based on the mean and standard deviation of the different metrics achieved through the LOOCV-based experimentation. **Table 10** summarizes the results, showing the mean and standard deviation of the different metrics over the training and testing sets for all DNN configurations. In this case, the best mean and standard deviation of MSE on the testing set were achieved by DNN7 with

Table 10. Statistical summary of various regression metrics from leave-one-out cross-validation applied to the 48 proposed DNN models.

Model	MAE				MSE				R^2	
	tr_mean	tr_std	te_mean	te_std	tr_mean	tr_std	te_mean	te_std	tr_mean	tr_std
DNN1-adadelta	50.9922	32.6245	49.5381	39.3609	401.5611	3237.9037	3974.6176	416.8091	−5.6675	5.3766
DNN1-adagrad	11.2924	0.6654	13.7992	10.4999	198.7792	20.3848	29.8626	442.2535	0.6702	0.0339
DNN1-adam	5.3533	3.2181	7.2245	8.1581	66.5104	6.5471	11.7515	248.1671	0.8896	0.1086
DNN1-adamw	4.7891	0.2634	5.2642	5.8317	53.0732	53.7865	6.1091	143.2394	0.9119	0.0892
DNN1-nadam	5.3796	3.3299	6.8788	0.6269	67.1972	67.1882	85.8894	12.7542	0.8886	0.1112
DNN1-rmsprop	5.4929	3.4285	7.2592	7.9887	65.4862	69.6876	115.3333	294.9952	0.8913	0.1157
DNN2-adadelta	11.8106	0.7966	13.6238	9.7872	206.4132	24.1601	279.6229	328.7262	0.6575	0.0399
DNN2-adagrad	10.7738	0.1293	13.5097	9.4021	175.8813	3.1757	269.2747	366.2304	0.7082	0.0052
DNN2-adam	1.7621	0.8056	2.2136	2.1222	6.7893	7.8156	9.3208	16.5868	0.9887	0.0129
DNN2-adamw	1.9046	0.7239	2.3783	2.7331	7.5543	6.1451	12.9878	30.3619	0.9875	0.0102

Table 10. Continued.

Model	MAE				MSE				R^2	
	tr_mean	tr_std	te_mean	te_std	tr_mean	tr_std	te_mean	te_std	tr_mean	tr_std
DNN2-nadam	2.0112	1.4553	2.7991	4.0666	10.0167	24.2197	24.0657	105.6014	0.9833	0.0408
DNN2-rmsprop	2.7768	1.7919	3.2635	3.2934	16.4467	29.5036	21.2962	47.6411	0.9727	0.0488
DNN3-adadelta	11.5451	0.5825	14.2736	9.9962	196.3148	16.8218	301.8093	394.3578	0.6742	0.0282
DNN3-adagrad	10.7349	0.1348	13.2794	9.2699	173.8966	4.1163	260.6829	348.8432	0.7115	0.0066
DNN3-adam	1.7133	0.7786	2.4219	0.2323	5.8046	6.0336	11.1616	17.3169	0.9904	0.0001
DNN3-adamw	2.0883	1.6362	3.2379	3.7938	11.7953	26.9025	24.6101	77.1551	0.9805	0.0445
DNN3-nadam	1.9408	1.3548	2.5206	2.3747	8.2514	13.6869	11.8885	19.0373	0.9863	0.0227
DNN3-rmsprop	2.6688	1.8496	3.6662	4.0771	14.2584	23.4905	29.7559	76.9126	0.9764	0.0388
DNN4-adadelta	13.8527	12.0437	1.4697	1.1668	422.9861	1134.8529	349.6237	630.5853	0.2959	1.8978
DNN4-adagrad	10.6622	0.0753	13.3829	9.4697	177.4426	2.3987	267.1178	38.3555	0.7056	0.0036
DNN4-adam	2.9991	2.1477	4.5112	4.7449	2.3644	36.4533	42.4482	92.6007	0.9608	0.0603
DNN4-adamw	2.9023	1.7748	3.6638	3.9994	21.4945	28.1068	29.1229	70.1256	0.9644	0.0465
DNN4-nadam	2.4808	1.2767	3.0599	3.2317	14.8967	17.5116	19.6136	38.7981	0.9753	0.0029
DNN4-rmsprop	0.4723	3.4202	0.0534	5.6283	49.8536	65.9656	5.9607	11.9906	0.9174	0.1093
DNN5-adadelta	11.8177	0.5791	14.7701	9.2137	203.1575	21.1933	301.4777	33.1883	0.6629	0.0351
DNN5-adagrad	10.5774	0.1143	13.2625	9.3306	17.1585	4.0545	261.3425	363.1245	0.7153	0.0068
DNN5-adam	1.5389	0.5656	2.4537	2.0629	0.4347	3.2928	10.1976	1.4289	0.9928	0.0055
DNN5-adamw	1.4226	0.4849	2.0169	2.0652	0.4021	0.3028	8.2538	15.6665	0.9933	0.0005
DNN5-nadam	2.0941	0.9908	2.4278	1.8312	7.5508	6.7223	9.1853	13.4595	0.9875	0.0112
DNN5-rmsprop	2.9162	1.6507	0.3481	2.6561	14.5282	15.2845	19.0415	26.0779	0.9759	0.0254
DNN6-adadelta	11.3664	0.3433	13.9118	0.9638	187.2094	9.6878	284.7099	339.2216	0.6894	0.0154
DNN6-adagrad	0.9123	0.4984	11.4986	8.7206	129.7374	12.6769	206.8588	288.7897	0.7847	0.0213
DNN6-adam	1.1439	0.4815	1.8803	1.5261	2.4417	0.2092	5.8214	8.9435	0.9959	0.0035
DNN6-adamw	1.2349	0.0597	1.8709	0.1628	2.7888	2.6075	6.1017	10.3222	0.9954	0.0043
DNN6-nadam	1.8021	1.3732	2.3001	1.8111	6.4672	9.7747	8.5098	11.8879	0.9893	0.0162
DNN6-rmsprop	2.5259	1.4032	2.9499	2.2816	1.0423	9.9408	13.8111	19.5811	0.9827	0.0165
DNN7-adadelta	10.8197	0.2247	13.4662	9.1385	172.9935	5.7291	263.3041	331.7588	0.0713	0.0091
DNN7-adagrad	4.1045	0.3572	4.8566	6.0102	41.3821	0.3547	59.0402	149.7733	0.9313	0.0059
DNN7-adam	1.6329	1.3335	2.2694	2.3008	5.4638	10.8842	10.3456	22.5247	0.9909	0.0181
DNN7-adamw	1.1887	0.5921	1.8164	1.4024	2.5918	2.2762	5.2296	7.2757	0.9957	0.0038
DNN7-nadam	0.1273	0.7756	1.8264	1.5723	2.9973	3.3310	5.7620	8.7274	0.0995	0.0055
DNN7-rmsprop	2.7564	1.7798	3.1216	2.7497	13.0283	17.0494	17.1656	32.1084	0.9784	0.0282
DNN8-adadelta	10.6556	0.0231	12.9729	8.9338	169.0319	5.9556	246.6296	314.4291	0.7195	0.0098
DNN8-adagrad	4.1471	0.2989	4.8484	6.3724	42.5252	4.2155	63.3623	168.7884	0.9294	0.0069
DNN8-adam	1.3248	0.6157	1.8055	1.5498	3.0023	2.6396	5.6173	10.1449	0.0995	0.0044
DNN8-adamw	1.5393	1.0043	1.8283	1.8279	4.5553	6.5934	6.6222	13.1932	0.9924	0.0109
DNN8-nadam	1.4377	0.9478	1.9134	1.9367	3.7966	5.9354	7.3425	14.2305	0.9937	0.0098
DNN8-rmsprop	0.3433	1.8514	4.0317	2.9694	18.1931	17.0899	24.9086	33.0177	0.9698	0.0283

the AdamW optimizer (in green). The results of this model across different metrics are similar for both the training and testing sets, which suggests that it does not suffer from overfitting. However, it is noticeable that the standard deviations are greater than in the previous experiment. This could be the result of the combination of real data and augmented data, as pointed out in ref. [40], where it is observed that synthetic data generators produce higher variance in results. The DNN1 with the Adadelta optimizer (in red) produces the worst results for both the mean and standard deviation of MSE on the testing set. It can be argued that this model suffers from underfitting, and across several runs, it is unstable due to the high standard deviation values.

6. Conclusion

The field of AI is vast; however, many of its techniques require fine parameter tuning tailored to the specific application. In our particular case, we have chosen to tackle the modeling of the behavior of an ultrafast pulsed laser in material characterization, particularly in oxide formation on a molybdenum film, which holds significant relevance in semiconductor manufacturing. We have opted to explore the use of DNNs, although other methods could also be applied. The choice of this technique stems from its widespread adoption, extensive available information, and readily available libraries. Moreover, its conceptual simplicity makes it accessible even to nonexperts in the field of AI.

Given the lack of a mathematical explanation guiding the selection of the number of layers and neurons in a neural network or the optimal optimizer, we decided to conduct thorough experimentation to enhance the robustness of our research. To this end, we initiated experimentation with an experimental setup where data was collected. These data were artificially augmented using interpolation, providing us with more information to train different models. In particular, we created 8 different neural network architectures, each with a minimum of 3 hidden layers. Additionally, we explored 6 different optimizers and varied the learning rate parameter, which serves as an indicator of fine adjustment during training.

All this experimentation was validated using statistical measures, including basic ones like MSE and MAE, as well as more sophisticated measures in the field of AI, such as the R^2 score. This score allows us to better understand the ability of our models to capture the behavior of our data.

Moreover, the generalizability of our models to other laser configurations or material types was a key consideration in our study. The physical basis of the laser-matter interaction was critical in guiding our neural network design. For instance, in the specific case of an 800 nm pulsed laser, the heat propagation distance during a 60 fs pulse is ≈2 nm due to diffusion effects, with an optical penetration depth of 20 nm—representing only 4% of the total film thickness. These precise dynamics highlight the importance of carefully tuning parameters when applying our models to other systems. While our focus was on molybdenum, the versatility of femtosecond laser interactions and the adaptability of DNNs suggest the potential for extending our methodology to other materials and laser wavelengths by modifying input parameters.

In conclusion, the versatility of our approach allowed us to explore a wide array of numerical configurations, systematically varying parameters and conditions, before committing to real-world experimentation. By doing so, we mitigated the inherent risks and resource expenditures associated with experimental trials, effectively minimizing errors and material wastage. Additionally, this computational approach afforded us the flexibility to refine and optimize our experimental design iteratively, leveraging insights gained from simulated scenarios to inform and enhance subsequent experimental iterations. Ultimately, this integrated computational-experimental approach empowered us to conduct more efficient and cost-effective research, accelerating progress in our understanding of material irradiation processes and paving the way for broader applications of laser-driven material transformations.

Acknowledgements

This research has been supported by the National Council of Humanities, Sciences, and Technology of Mexico (CONAHCYT) through the scholarship 916172.

Conflict of Interest

The authors declare no conflict of interest.

Author Contributions

Jose R. Paredes-Miguel: data curation (equal); investigation (equal); methodology (equal); software (equal); validation (equal); writing—original draft (equal). **Miroslava Cano-Lara**: conceptualization (equal); formal analysis (equal); investigation (equal); software (equal); supervision (equal); writing—original draft (equal); writing—review and editing (equal). **Andres A. Garcia-Granada**: conceptualization (equal); formal analysis (equal); investigation (equal); methodology (equal); writing—original draft (equal). **Andres Espinal**: data curation (equal); methodology (equal); software (equal); visualization (equal); writing—original draft (equal). **Marcos J. Villaseñor-Aguilar**: data curation (equal); investigation (equal); project administration (equal); software (equal); validation (equal); writing—review and editing (supporting). **Leonardo Martinez-Jimenez**: data curation (equal); formal analysis (equal); investigation (equal); methodology (equal); software (equal); writing—original draft (equal). **Horacio Rostro-Gonzalez**: conceptualization (lead); formal analysis (equal); funding acquisition (lead); supervision (lead); writing—original draft (lead); writing—review and editing (lead).

Data Availability Statement

The data and code that support the findings of this study can be found in the following link: https://github.com/BioInspiredLab-UGTO/DNN-BASED_FS_LASER_PULSED.

Keywords

deep neural networks, material characterization, molybdenum thin films, oxide formation, ultrafast pulsed lasers

Received: July 5, 2024
Revised: February 15, 2025
Published online: April 10, 2025

[1] Y. Zhang, D. Wu, Y. Zhang, Y. Bian, C. Wang, J. Li, J. Chu, Y. Hu, *Int. J. Extreme Manuf.* **2023**, *5*, 042012.
[2] A. B. Kaligar, H. A. Kumar, A. Ali, W. Abuzaid, M. Egilmez, M. Alkhader, F. Abed, A. S. Alnaser, *Quantum Beam Sci.* **2022**, *6*, 5.
[3] S. Lei, X. Zhao, X. Yu, A. Hu, S. Vukelic, M. B. G. Jun, H.-E. Joe, Y. L. Yao, Y. C. Shin, *J. Manuf. Sci. Eng.* **2020**, *142*, 031005.
[4] M. Malinauskas, A. Žukauskas, S. Hasegawa, Y. Hayasaki, V. Mizeikis, R. Buividas, S. Juodkazis, *Light: Sci. Appl.* **2016**, *5*, e16133.
[5] X. Sedao, S. Papa II, S. Reynaud, N. Compère III, A. Guignandon II, V. Dumas IV, H. Reveron, J. Chevalier, F. Garrelie, Y. Di Maio, et al., in *Laser-Based Micro-and Nanoprocessing XVI*, SPIE, San Francisco, California, United States **2022**, p. PC119890H.
[6] L. Orazi, L. Romoli, M. Schmidt, L. Li, *CIRP Ann.* **2021**, *70*, 543.
[7] J.-X. Zheng, K.-S. Tian, J.-Y. Qi, M.-R. Guo, X.-Q. Liu, *Opt. Laser Technol.* **2023**, *167*, 109793.

[8] M. Anderson, A. Ediger, A. Tsubaki, C. Zuhlke, D. Alexander, G. Gogos, J. E. Shield, *Surf. Coat. Technol.* **2021**, *409*, 126872.
[9] D. S. Correa, J. M. P. Almeida, G. F. B. Almeida, M. R. Cardoso, L. De Boni, C. R. Mendonça, *Photonics* **2017**, *4*, 8.
[10] K. Sugioka, Y. Cheng, *Light: Sci. Appl.* **2014**, *3*, e149.
[11] M. Cano-Lara, S. Camacho-López, A. Esparza-García, M. Camacho-López, *Opt. Mater.* **2011**, *33*, 1648.
[12] J. Bonse, J. Krüger, *Appl. Phys. A* **2022**, *129*, 14.
[13] S. Camacho-Lopez, M. Cano-Lara, M. Camacho-Lopez, *Crystals* **2020**, *10*, 629.
[14] H. Zhang, A. Antoncecchi, S. Edward, P. Planken, S. Witte, in *2019 Conf. Lasers and Electro-Optics Europe & European Quantum Electronics Conf. (CLEO/Europe-EQEC)*, Munich, Germany **2019**, p. 1.
[15] D. Zhu, P. Zuo, F. Li, H. Tian, T. Liu, L. Hu, H. Huang, J. Liu, X. Qian, *Colloid Interface Sci. Commun.* **2024**, *59*, 100770.
[16] L. Jiang, A.-D. Wang, B. Li, T.-H. Cui, Y.-F. Lu, *Light: Sci. Appl.* **2018**, *7*, 17134.
[17] E. Stratakis, A. Ranella, M. Farsari, C. Fotakis, *Prog. Quantum Electron.* **2009**, *33*, 127.
[18] S. Camacho-Lopez, I. O. Perez-Lopez, M. Cano-Lara, A. Esparza-Garcia, M. C. Maya-Sanchez, J. A. Reynoso-Hernandez, M. Camacho-Lopez, *Phys. Status Solidi A* **2018**, *215*, 1800226.
[19] O. Concepción, O. de Melo, *J. Phys.: Condens. Matter* **2023**, *35*, 143002.
[20] N. Makeswaran, C. Orozco, A. K. Battu, E. Deemer, C. V. Ramana, *Materials* **2022**, *15*, 3.
[21] H. Kim, B. Anasori, Y. Gogotsi, H. N. Alshareef, *Chem. Mater.* **2017**, *29*, 6472.
[22] G. Zhu, J. Liu, Q. Zheng, R. Zhang, D. Li, D. Banerjee, D. G. Cahill, *Nat. Commun.* **2016**, *7*, 13211.
[23] H. Rashid, K. S. Rahman, M. I. Hossain, A. A. Nasser, F. H. Alharbi, M. Akhtaruzzaman, N. Amin, *Results Phys.* **2019**, *14*, 102515.
[24] D. D. Xia, F. Gong, X. Pei, W. Wang, H. Li, W. Zeng, M. Wu, D. V. Papavassiliou, *Chem. Eng. J.* **2018**, *348*, 908.
[25] S. Hu, N. S. Lewis, J. W. Ager, J. Yang, J. R. McKone, N. C. Strandwitz, *J. Phys. Chem. C* **2015**, *119*, 24201.
[26] K. C. Phillips, H. H. Gandhi, E. Mazur, S. K. Sundaram, *Adv. Opt. Photonics* **2015**, *7*, 684.
[27] B. Duan, B. Wu, J.-H. Chen, H. Chen, D.-Q. Yang, *Front. Mater.* **2022**, *8*, 791296.
[28] R. Thomas, E. Westphal, G. Schnell, H. Seitz, *Micromachines* **2024**, *15*, 491.
[29] J. Theerthagiri, K. Karuppasamy, S. J. Lee, R. Shwetharani, H.-S. Kim, S. K. K. Pasha, M. Ashokkumar, M. Y. Choi, *Light: Sci. Appl.* **2022**, *11*, 250.
[30] L. Alzubaidi, J. Zhang, A. J. Humaidi, A. Al-Dujaili, Y. Duan, O. Al-Shamma, J. Santamaría, M. A. Fadhel, M. Al-Amidie, L. Farhan, *J. Big Data* **2021**, *8*, 53.
[31] J. A. Grant-Jacob, B. Mills, M. N. Zervas, *Manuf. Lett.* **2023**, *38*, 11.
[32] D. Piccinotti, K. F. MacDonald, S. A. Gregory, I. Youngs, N. I. Zheludev, *Rep. Prog. Phys.* **2021**, *84*, 012401.
[33] W. Ma, Z. Liu, Z. A. Kudyshev, A. Boltasseva, W. Cai, Y. Liu, *Nat. Photonics* **2021**, *15*, 77.
[34] F. P. Sunny, E. Taheri, M. Nikdast, S. Pasricha, *ACM J. Emerging Technol. Comput. Syst.* **2021**, *17*, 1.
[35] L. Baronti, A. Michalek, M. Castellani, P. Penchev, T. L. See, S. Dimov, *Int. J. Adv. Manuf. Technol.* **2022**, *119*, 3501.
[36] S. P. Mishra, M. Rahul, *Mater. Chem. Phys.* **2023**, *308*, 128275.
[37] K. Choudhary, B. DeCost, C. Chen, A. Jain, F. Tavazza, R. Cohn, C. W. Park, A. Choudhary, A. Agrawal, S. J. L. Billinge, E. Holm, S. P. Ong, C. Wolverton, *npj Comput. Mater.* **2022**, *8*, 59.
[38] M. L. Lau, A. Burleigh, J. Terry, M. Long, *J. Vac. Sci. Technol., A* **2023**, *41*, 060801.
[39] H. K. Kim, M. Woo, H. Ki, *Mater. Des.* **2023**, *226*, 111639.
[40] M. R. Santander, J. H. Albarracin, A. R. Rivera, *Expert Syst. Appl.* **2021**, *183*, 114991.
[41] A. Mumuni, F. Mumuni, *Array* **2022**, *16*, 100258.
[42] J. Li, W. Wan, Y. Feng, J. Chen, *Comput. Ind.* **2025**, *165*, 104226.
[43] P. Seth, A. Bhandari, K. Lakara, *Analyzing Effects of Fake Training Data on the Performance of Deep Learning Systems*, https://arxiv.org/abs/2303.01268 (accessed: October 2023).